



Optics Letters

Long focusing range and self-healing Bessel vortex beam generator

ZHI-YONG HU,¹ ZHEN-NAN TIAN,^{1,3}  HUA FAN,¹ JIAN-GUAN HUA,¹ MENG-DAN QIAN,¹ QI-DAI CHEN,¹ AND HONG-BO SUN^{1,2,4} 

¹State Key Laboratory of Integrated Optoelectronics, College of Electronic Science and Engineering, Jilin University, 2699 Qianjin Street, Changchun 130012, China

²State Key Laboratory of Precision Measurement Technology and Instruments, Department of Precision Instrument, Tsinghua University, Haidian, Beijing 100084, China

³e-mail: zhennan_tian@jlu.edu.cn

⁴e-mail: hbsun@tsinghua.edu.cn

Received 25 February 2020; revised 21 March 2020; accepted 3 April 2020; posted 6 April 2020 (Doc. ID 391232); published 27 April 2020

Here a continuous axial-spiral phase microplate (CAsPP), based on combining a logarithmic axicon and a spiral phase plate, was proposed for generating high-quality higher-order Bessel vortex beams. The novel optical component implemented via femtosecond laser direct writing possesses compact geometry and unique optical properties. The CAsPP with a diameter of 80 μm possesses a controllable long focus ranging from 50 to 600 μm and exhibits a good self-healing ability after free transmission of about 45 μm . Unique optical properties were demonstrated in both experiments and simulations, which were well matched to each other. This Letter provides new opportunities for applications in integrated optics, optical trapping, laser machining, and information reconstruction. © 2020 Optical Society of America

<https://doi.org/10.1364/OL.391232>

In the field of optics, a light's wavefront with an intentional helical defect rotates spirally along the optical axis, forming an optical vortex (OV). Due to its special phase structure, the OV beam possesses the characteristics of zero central intensity and carrying the orbital angular momentum (OAM). Benefitting from their unique optical properties, since discovered by Allen in 1992 [1], OV beams have shown great potential in particle manipulation [2], super-resolution imaging [3], and data transmission [4–6]. The higher-order Bessel vortex beam (HoBVB), as a special vortex beam, has become a very important frontier research hotspot in optical fields due to its characteristics of non-diffraction [7] and self-healing [8]. Moreover, Chen *et al.* first reported that it can bring an optical pulling force, which successfully increased optical manipulation freedom [9]. By far, the most common method for generating HoBVBs is to load computational holograms via a spatial light modulator (SLM) [10,11]. This method has high flexibility, but there are problems such as large size, high cost, and low withstand power. Laser resonators are also customized to produce HoBVBs [12], while their need of a pump light source makes the system complicated and bulky. Incident Gaussian beams can be converted

into Bessel modes by metasurfaces as well [13], still limited by complicated design, difficult manufacture, and expensive cost.

Another straightforward way to generate HoBVBs is to illuminate axicons with Laguerre–Gaussian (LG) beams [14]. However, appropriate illuminating light of the LG mode requires additional pathways such as computational holographic technology [15], diffractive optical elements (DOEs) [16,17], cylindrical lens mode conversion [18], and laser cavities [19]. Currently, generating HoBVBs with axicons is basically completed by a macro combination system, in which the separate device's size is above the millimeter level. This kind of method will bring tedious operations, large size, and alignment error, which is not applicable for integrated optics. For the further development of HoBVBs in integrated optics, Žukauskas *et al.* seamlessly connected a DOE and axicon reversely [20], and Balcytis *et al.* integrated a dielectric axicon and a metal spiral phase plate (SPP) [21] to generate HoBVBs, effectively reducing the combined system's volume; Oliveira *et al.* designed a micron-sized DOE based on a circular grating and a SPP to generate HoBVBs [22].

Herein, we designed a novel DOE continuous axial-spiral phase microplate (CAsPP). The device, whose actual profile basically matches the design, was prepared by femtosecond laser direct writing (FsLDW). It is suitable for generating high-quality HoBVBs in various integrated optical systems. Our experiments demonstrated that the fabricated CAsPP generated HoBVBs carrying different OAMs, with a long focusing range (50–600 μm). The diameter of the experimental focus deviated from the calculation by less than 5%. Moreover, the reconstruction processes after the destruction of focused Bessel OVs, and letters were systematically investigated, demonstrating the self-healing characteristic.

It is well known that axicons can produce approximate zero-order Bessel beams with long foci. Furthermore, the logarithmic axicon (LA) [23] with a logarithmic type surface can inhibit the divergence angle of traditional axicons when focusing, thereby obtaining a more uniform intensity distribution on the focal line. Here the CAsPP was designed by combining the phases of the LA and SPP, so as to obtain the axial spiral phase

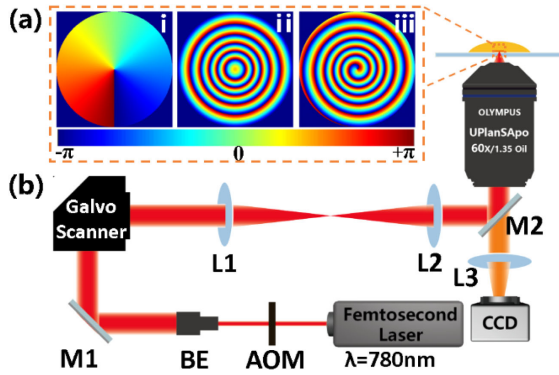


Fig. 1. Galvanometer-based femtosecond laser processing system and calculation process of CAsPP phase distribution. (a) Phase distribution. i, SPP; ii, logarithmic axicon; iii, micro-vortex beam generator. (b) Schematic of processing system. AOM, acousto-optic modulator; BE, beam expander; M, mirror; L, lens; CCD, charge-coupled device.

distribution. The phase function of the SPP can be described as

$$\psi_{\text{SPP}}(r, \theta) = \exp(i l \theta). \quad (1)$$

The forward logarithmic axicon's phase function can be written as

$$a = \frac{(d_2 - d_1)}{R^2}, \quad (2)$$

$$\psi_{\text{LA}}(r, \theta) = -\frac{1}{2a} \ln \left\{ 2a \left[a^2 r^4 + (1 - 2ad_2) r^2 + d_2^2 \right]^{\frac{1}{2}} + 2a^2 r^2 + 1 - 2ad_2 \right\}, \quad (3)$$

where r , θ , and l represent the radius coordinate, azimuthal coordinate, and topological charge, respectively. d_1 and d_2 are the start and end points of the focal line, and R is the element's radius.

The phase function of the CAsPP is obtained by combining the phase functions of the SPP [Eq. (1)] and LA [Eq. (3)]:

$$\psi_{\text{CAsPP}}(r, \theta) = \psi_{\text{SPP}}(r, \theta) \times \psi_{\text{LA}}(r, \theta). \quad (4)$$

The phase information of elements mentioned above is shown in Fig. 1(a), where i is the phase distribution of the SPP with a topological charge of one. As the rotation angle changes from 0° to 360° , the phase changes from $-\pi$ to $+\pi$. ii is the phase distribution of LA (focusing range: 50–600 μm), wrapped between 0 and 2π with a phase change of 11.36π , according to Eq. (3). The phase of the CAsPP obtained by phase superposition is shown in Fig. 1(a) iii. Theoretically, a focused OV will be obtained at the position of 50 to 600 μm on the optical axis when a planar light passes through the phase element.

CAsPPs were prepared by FsLDW which is a well-known high-precision 3D machining technology [24–27]. Here we used a homemade femtosecond laser processing system. Figure 1(b) displays the optical path. The femtosecond laser (center wavelength, 780 nm; pulse width, 100 fs; repetition frequency, 80 MHz) first passes through the acousto-optic modulator with 70 MHz switching frequency. Next, the beam

is expanded five times with the beam expander (BE), and then the beam deflection is controlled via the galvanometer at high speed. Finally, the beam is focused tightly into the polymer via using a high numerical aperture (NA) objective lens (Olympus UPlanSApo 60 \times , NA-1.35, Oil), thereby utilizing the material's two-photon absorption (TPA) effect to achieve subwavelength processing resolution. Meanwhile, the real-time monitoring system is mainly formed by a yellow light (not absorbed by the material), a glass lens, and a highly sensitive charge-coupled device (CCD).

Experimental resin is a new type of organic-inorganic hybrid polymer [SZ-2080 (IESL-FORTH)] with ultra-low shrinkage [28]. To improve the TPA effect, a 1 wt. % photosensitizer 4,4-Bis(diethylamino)benzophenone was mingled with the resin. It is known that the relation between phase and optical path difference is expressed as

$$\Delta\varphi = \Delta n h * \frac{2\pi}{\lambda}. \quad (5)$$

The refractive index of polymerized resin was 1.5, and the test light wavelength was 633 nm. The refractive index difference (Δn) from air was 0.5. Due to the phase wrapping, the phase change of a single sawtooth ring was 2π . According to Eq. (5), the height of the device was calculated to be 1.266 μm .

Figure 2 shows the fabrication results of CAsPPs (focusing range of 50–600 μm) with different topological charges. Figure 2(a) exhibits a scanning electron microscope (SEM, JSM-7500 F, JEOL) photos; Fig. 2(b) shows laser confocal microscopy (LSCM, OLS3000, EVC electronic) 3D images (45 $^\circ$ tiled view). The detailed experimental parameters are as follows: diameter 80 μm , height 1.266 μm , power in front of the objective lens 15 mw, and scanning speed 0.5 mm/s. The fabricated device has a complete structure, a good morphology, and high processing quality. The actual surface profile of the fabrication ($l = 1$) along the horizontal and vertical direction was extracted and compared with the theoretical design. The comparison results are shown in Fig. 2(c). The blue and red lines show the theoretical and experimental results, respectively, which are basically consistent with each other.

The focus of the OV beam is like a hollow ring due to the spiral wavefront and phase singularity. A tightly focused laser creates an optical ring trap that could be used for optical particle manipulation. The size of the hollow ring related to the topological charges is an important parameter for optical trapping. Figure 3(a) exhibits the simulation results of CAsPP energy distributions (50–600 μm) with topological charges of 1, 2, and 3 in the focus plane ($Z = 360 \mu\text{m}$). Figure 3(b) is the corresponding experimental results of the energy distributions. Figures 3(c) and 3(d) show interferograms of the simulation and experiment in the X–Y plane (slightly in front of the focus plane). A program based on the fast Fourier transform algorithm was applied to calculate theoretical results on the MATLAB platform. A coaxial interference optical system uses the interference between a spherical wave and the target beam produced by CAsPPs to detect the beam's topological charge information. To further characterize the energy distributions of focused light fields, we extracted the energy of the foci along horizontal and vertical directions. A normalized energy curve is shown in Fig. 3(e). Besides, Fig. 3(e) iv shows theoretical and experimental focus diameters at different topological charges. It is worth noting that the actual diameters of the focused hollow rings with different

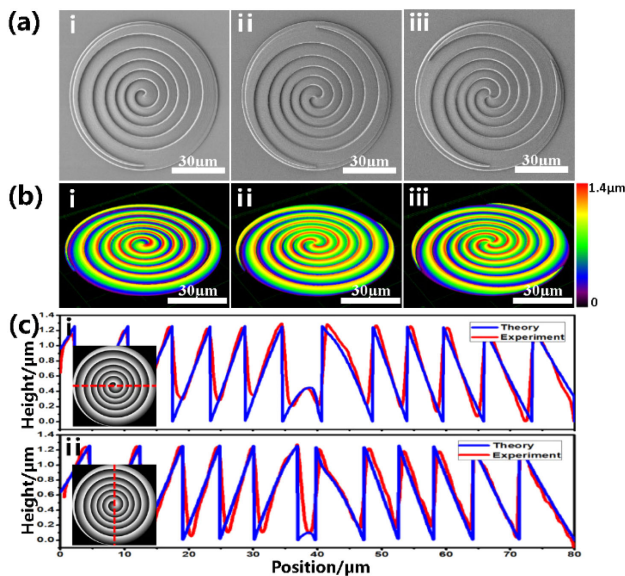


Fig. 2. Fabrication results of CASPPs (focusing range of 50–600 μm) with various topological charges. (a) SEM images. i, $l = 1$; ii, $l = 2$; iii, $l = 3$. (b) Laser confocal microscopy 3D images. (c) Surface profile of (b)-iii. The blue and red lines separately correspond to the theoretical and experimental results, respectively. The illustration displays the corresponding extraction position of the section profile. i, horizontal; ii, vertical.

topological charges were 4.11, 6.40, and 9.08 μm , and the corresponding theoretical sizes were 4.06, 6.72, and 9.45 μm . The error between the experimental and simulated diameters was less than 5%. The experimental results were basically consistent with the theoretical simulations.

The introduction of LA enables CASPPs to adjust the position and length of the focus, which were limited by preparation feasibility and peak intensity. To prove the programmable focal length characteristics of CASPPs, we manufactured components with different focal lengths. Figure 4 exhibits the theoretical and experimental results, wherein (a), (b), and (c) correspond to CASPPs with a focal length range of 100–300, 300–500, and 50–600 μm , respectively. In each dotted box, i characterizes the phase information, and ii shows SEM images of the devices; iii and iv are the theoretical and test results of the focal light field energy distributions in the X–Z plane. Meanwhile, as shown in Fig. 4, the device shows a uniform axial intensity distribution, which is significant in practical applications [29]. The results of the experiments matched well with the theoretical designs. To conclude, the evidence has shown so far that CASPPs can indeed produce long circular foci, and the focal length and the focusing position can be adjusted easily by parameters in Eq. (3). This provides new insights into optical trapping of irregular particles such as nanowires, high aspect ratio lithography, and rapid processing of structured light field based on SLM.

To investigate self-healing properties of HoVBVs and Bessel letters generated by the CASPPs, a series of related experiments were performed. Figure 5(a) displays the corresponding testing setup schematic, in which a He-Ne laser (wavelength of 632.8 nm) was used as a testing light source. The reconstructions of partially blocked focused OVVs and Bessel letters after different propagation distances were observed. First, three different shapes of barriers, which were obtained by ablating the

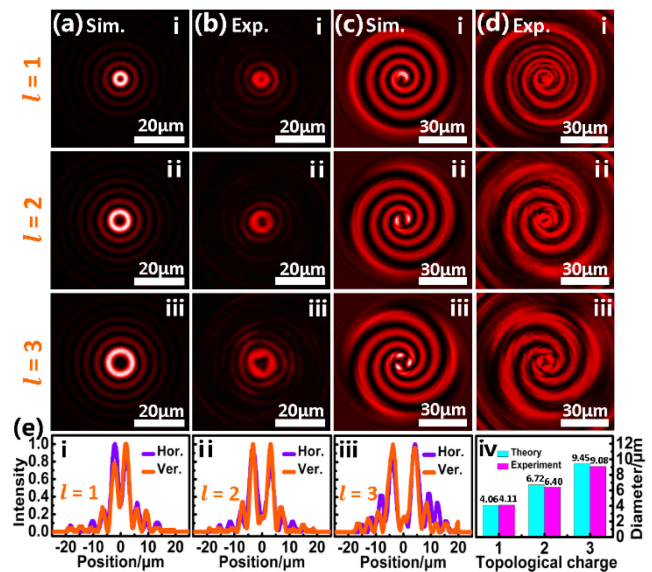


Fig. 3. Numerical simulations and experimental results of CASPPs (50–600 μm) in the X–Y plane. (a) Simulated and (b) measured intensity distributions; (c) simulated and (d) measured interferograms in the X–Y plane ($Z = 360 \mu\text{m}$). i, $l = 1$; ii, $l = 2$; iii, $l = 3$. (e) Normalized energy distributions along horizontal and vertical directions of foci. i, ii, and iii correspond to (b)-i, ii, and iii. iv shows theoretical and experimental focus diameters at different topological charges.

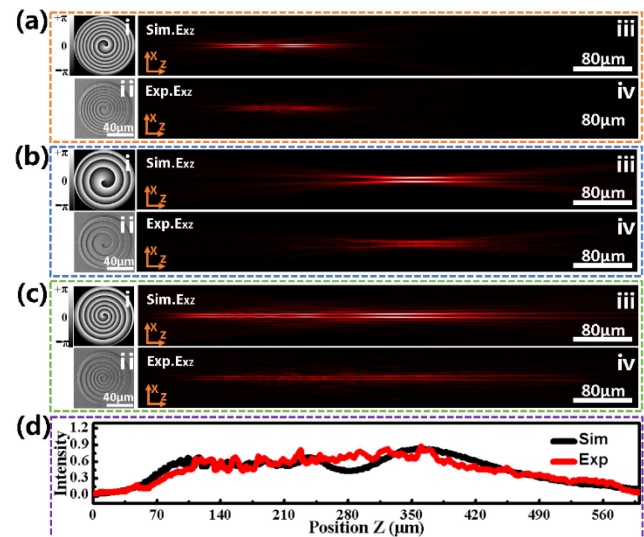


Fig. 4. Simulated and experimental axial intensities of CASPPs. Intensity distribution in the X–Z plane: focal length range (a) 100–300, (b) 300–500, and (c) 50–600 μm . i, phase information; ii, SEM images; iii, simulated and iv, measured energy distribution in the X–Z plane. (d) Corresponding uniform axial intensity curves (50–600 μm) of the simulation and the experiment in the Y–Z plane.

microscope cover glass surface with a high-power femtosecond laser (scanned area for blocking), were placed at the starting position of focusing in the order of the occlusion area getting larger. Figure 5(b) illustrates photos of the focused OVVs before being blocked and after being blocked propagating 0, 22.5, 52.5, 75, and 112.5 μm . The basic and complete repairs of OVVs

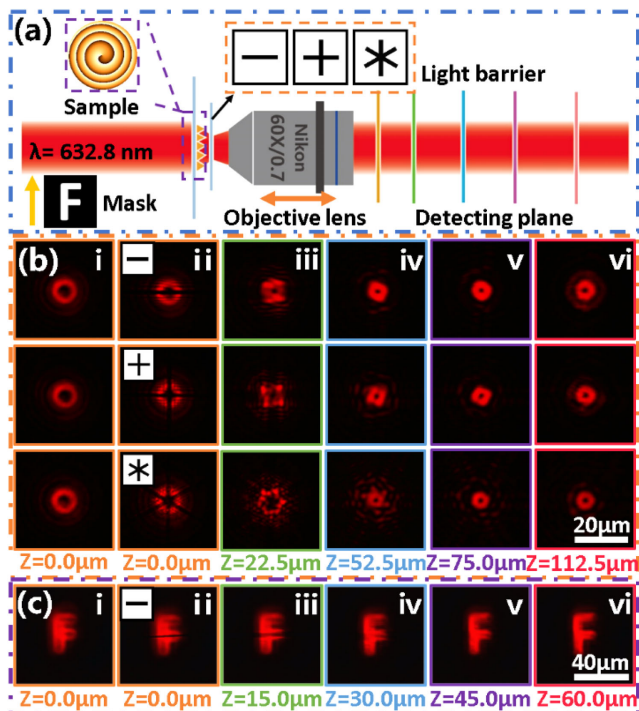


Fig. 5. Characterization of self-healing properties. (a) Schematic of exploring the self-healing ability of OVs and Bessel letters. (b) Demonstration of focusing OVs self-healing process under the obstruction of different light barriers. (c) Reconstruction of Bessel letter F after being destroyed. i, detecting results before obstruction; ii–vi, detecting results after obstruction.

were observed after propagating 52.5 and 75 μm , respectively. In addition, we focused the millimeter-sized mask of the hollow-out letter F in front of the CAsPP with an objective lens. The letter information will be loaded on the device's Fourier plane after Fraunhofer diffraction, and then the Bessel letter F can be observed after the objective lens's Fourier transform [30]. Meanwhile, the reconstruction process of the Bessel letter F was investigated shown in Fig. 5(c). The destroyed letter F was successfully repaired after spreading 45 μm . The above results demonstrate that both the OV and Bessel letter generated by the CAsPP have self-healing properties, which can be utilized for transferring lossless information.

In summary, we designed and fabricated a novel high-quality HoBVB generator (CAsPP) with a precise size (diameter of 80 μm , height of 1.266 μm). The device implemented via FsLDW has a continuous and match-designed surface profile, which mainly determines the device performance. Optical properties such as carrying arbitrary OAMs and a long focusing range (50–600 μm) were demonstrated in both experiments and simulations, which agreed well with each other. Simultaneously, the self-healing properties of OVs and Bessel letters generated by CAsPPs were verified experimentally (successfully repaired after propagating 45 μm). The HoBVB generator has the characteristics of simple structure, programmable design, easy preparation, and high integration. Additionally, it has great application potential in optical manipulation, quantum coding communication, structured light field machining, and lossless information transmission.

Funding. National Key Research and Development Program of China (2017YFB1104600); National Natural Science Foundation of China (61825502, 61590930, 61827826, 21903035).

Disclosures. The authors declare no conflicts of interest.

REFERENCES

1. L. Allen, M. W. Beijersbergen, R. Spreeuw, and J. Woerdman, *Phys. Rev. A* **45**, 8185 (1992).
2. Y. Shen, X. Wang, Z. Xie, C. Min, X. Fu, Q. Liu, M. Gong, and X. Yuan, *Light Sci. Appl.* **8**, 90 (2019).
3. L. Li and F. Li, *Phys. Rev. E* **88**, 033205 (2013).
4. L. Gong, Q. Zhao, H. Zhang, X. Y. Hu, K. Huang, J. M. Yang, and Y. M. Li, *Light Sci. Appl.* **8**, 27 (2019).
5. Z. Zhang, X. Liang, M. Goutsoulas, D. Li, X. Yang, S. Yin, J. Xu, D. N. Christodoulides, N. K. Efremidis, and Z. Chen, *APL Photonics* **4**, 076103 (2019).
6. C. Vetter, R. Steinkopf, K. Bergner, M. Ornigotti, S. Nolte, H. Gross, and A. Szameit, *Laser Photonics Rev.* **13**, 1900103 (2019).
7. K. Kuntz, B. Braverman, S. Youn, M. Lobino, E. Pessina, and A. Lvovsky, *Phys. Rev. A* **79**, 043802 (2009).
8. F. O. Fahrbach, P. Simon, and A. Rohrbach, *Nat. Photonics* **4**, 780 (2010).
9. J. Chen, J. Ng, Z. Lin, and C. Chan, *Nat. Photonics* **5**, 531 (2011).
10. A. H. Dorrah, M. Zamboni-Rached, and M. Mojahedi, *Light Sci. Appl.* **7**, 40 (2018).
11. S. Ji, R. Li, Z. Cai, D. Pan, L. Yang, Y. Hu, J. Li, D. Wu, and J. Chu, *Opt. Lett.* **44**, 5073 (2019).
12. D. N. Schimpf, J. Schulte, W. P. Putnam, and F. Kärtner, *Opt. Express* **20**, 26852 (2012).
13. W. T. Chen, M. Khorasaninejad, A. Y. Zhu, J. Oh, R. C. Devlin, A. Zaidi, and F. Capasso, *Light Sci. Appl.* **6**, e16259 (2017).
14. J. Arit and K. J. O. C. Dholakia, *Opt. Commun.* **177**, 297 (2000).
15. T. Lu, T. Huang, J. Wang, L. Wang, and R. R. Alfano, *Sci. Rep.* **6**, 39657 (2016).
16. T. Lei, M. Zhang, Y. Li, P. Jia, G. N. Liu, X. Xu, Z. Li, C. Min, J. Lin, C. Yu, H. Niu, and X. Yuan, *Light Sci. Appl.* **4**, e257 (2015).
17. E. Brasselet, M. Malinauskas, A. Žukauskas, and S. Juodkazis, *Appl. Phys. Lett.* **97**, 211108 (2010).
18. X. Fang, Z. Kuang, P. Chen, H. Yang, Q. Li, W. Hu, Y. Lu, Y. Zhang, and M. Xiao, *Opt. Lett.* **42**, 4387 (2017).
19. G. Lin, Y. Cao, R. Ji, C. Hou, and Z. Lu, *Opt. Lett.* **43**, 4164 (2018).
20. A. Žukauskas, M. Malinauskas, and E. Brasselet, *Appl. Phys. Lett.* **103**, 181122 (2013).
21. A. Balcytis, D. Hakobyan, M. Gabalis, A. Žukauskas, D. Urbonas, M. Malinauskas, R. Petruskevicius, E. Brasselet, and S. Juodkazis, *Opt. Express* **24**, 16988 (2016).
22. J. M. Oliveira, A. J. Jesus Silva, and E. J. Fonseca, *Opt. Laser Technol.* **119**, 105632 (2019).
23. I. Golub, B. Chebbi, D. Shaw, and D. Nowacki, *Opt. Lett.* **35**, 2828 (2010).
24. X. Wang, A. A. Kuchmizhak, E. Brasselet, and S. Juodkazis, *Appl. Phys. Lett.* **110**, 181101 (2017).
25. Y. L. Zhang, Y. Tian, H. Wang, Z. C. Ma, D. D. Han, L. G. Niu, Q. D. Chen, and H. B. Sun, *ACS Nano* **13**, 4041 (2019).
26. H. Wang, Y. L. Zhang, W. Wang, H. Ding, and H. B. Sun, *Laser Photonics Rev.* **11**, 1600116 (2017).
27. Z. C. Ma, X. Y. Hu, Y. L. Zhang, X. Q. Liu, Z. S. Hou, L. G. Niu, L. Zhu, B. Han, Q. D. Chen, and H. B. Sun, *Adv. Funct. Mater.* **29**, 1903340 (2019).
28. D. Gailevičius, V. Padolskytė, L. Mikolūnaitė, S. Šakirzanovas, S. Juodkazis, and M. Malinauskas, *Nanoscale Horiz.* **4**, 647 (2019).
29. R. Dharmavarapu, S. Bhattacharya, and S. Juodkazis, *J. Opt.* **20**, 085606 (2018).
30. Z. Cai, Y. Liu, Y. Hu, C. Zhang, J. Xu, S. Ji, J. Ni, Z. Lao, J. Li, Y. Zhao, and D. Wu, *Opt. Lett.* **43**, 1151 (2018).